HiSST: 4th International Conference on High-Speed Vehicle Science & Technology

22–26 September 2025, Tours, France

CEAS
Council of European Aerospace Societies

Design and Analysis of Hypersonic Intakes for Dual-Mode Ramjet Engines

Luigi BELLOMO[1], Bayindir H SARACOGLU[2]

Abstract

Hypersonic air-propulsion propulsion promises a paradigm change in civil aviation and space access by radically increasing the travel speeds, exploiting higher flight altitudes and leveraging lifting airframes as well as horizontal take off an landing. However, the realizing hypersonic flight requires successful implementation of air-breathing propulsion system with all its vital components along the flow path starting from the air intake. Hypersonic vehicles necessitates seamless integration of the propulsion system on airframe due to harsh aero-thermal flight conditions as well as overall aero-propulsive efficiency of the entire system. Consequently, design of three-dimensional intakes is critical to achieve plausible hypersonic concepts that can eventually soar at stratospheric altitudes. Current study summaries a design methodology for highly 3D intakes starting from 2D analytical designs generated with the Taylor–Maccoll equations. Streamline tracing of the isolator profile following viscous corrections are then implemented to extract the final geometry by taking into account the effects of boundary layer developing over the long flow path from the leading edge to the combustor interface. The final 3D geometry was then numerically tested using 3D RANS simulations at on-design Mach 5 flight conditions at 25 km of altitude. Finally an exhaustive numerical camping was conducted to generate the performance characteristics matrix for the intake at off-design conditions.

Keywords: Hypersonic Flow, CFD, propulsions, Dual-mode ramjet, Shock wave, Busemann Intake

Nomenclature

Latin
DMR – Dual-Mode Ramjet
M_1 – Inlet Mach Number
M_3 – Exit Mach Number
r – Final intake radius at the exit
$RANS$ – Reynolds-Averaged Navier-Stokes

Greek
δ_t – Truncation Angle
η – Compression efficiency
α – Angle of Attack
β – Sideslip Angle
h – Altitude

1. Introduction

Hypersonic air-breathing propulsion research has attracted considerable attention as a viable method for sustained high-speed atmospheric flight. Dual-mode ramjet (DMR) engines, which operate with both subsonic and supersonic airflow through the combustor, offer a more efficient solution than traditional rocket and turbojet systems. By eliminating the need for onboard oxidizers and mechanical compression, DMRs can achieve higher specific impulse and simpler mechanical architecture, making them ideal for missions involving sustained hypersonic cruise or space access [1].

One of the most critical component of this propulsion system is the intake which is responsible to efficiently compress the incoming flow field through compression waves and oblique shocks and condition the incoming flow to ensure proper combustion downstream. At hypersonic speeds, this task is fairly complicated due to strong shock interactions, viscous effects, and the tight integration between the intake and the vehicle's aerodynamic structure. Effective intakes must achieve high compression ratios while minimizing total pressure losses and maintaining flow uniformity.

---

[1] Von Karman Institute for Fluid Dynamics, Belgium, luigi.bellomo@vki.ac.be
[2] Von Karman Institute for Fluid Dynamics, Belgium, bayindir.saracoglu@vki.ac.be

To address these challenges, intake design often begins with analytically defined, simplified flow models. Axisymmetric and conical Taylor–Maccoll flows provide a solid foundation for intake geometries, reducing the complexity of the design process. Among these, the Busemann intake is particularly efficient, as it compresses the flow primarily through convergence rather than shock deflection. This results in minimal entropy generation and better pressure recovery [2]. Experimental comparisons between Busemann, Oswatitsch, and Prandtl–Meyer intake designs demonstrate the Busemann type intake designs' superiority in maintaining efficiency under realistic viscous conditions [3]. Additionally, design techniques such as wavecatching allow for fine-tuned control of shock positioning and boundary layer management.

The performance characteristics of the Busemann intake have been extensively investigated, with Mölder and Van Wie [4] proposing its application to flight vehicles. A notable practical implementation can be found in the JHU/APL missile-type intake [5], which employed a four-module design based on the streamline tracing approach. This intake was integrated into a scramjet engine and successfully launched in Barbados in 1972. Further refinement and analysis of the four-module intake were conducted by Matthews and Jones [6], who explored its aerodynamic performance and design optimizations.

A series of European research projects funded by consecutive European Commissions Frame programs are devoted to investigate various hypersonic and supersonic civilian aircraft and two-stage-to-orbit concepts leveraging turbine-based combined cycle propulsion systems operating in air-breathing regime [7], [8], [9]. The latest of these projects include LAPCAT-II [7], STRATOFLY [10] and MOREandLESS [11] which considered highly 3D intake design seamlessly merging propulsion system with the airframe.

Given its performance advantages, the Busemann intake serves as the foundation of this study, which investigates its design and optimization for Mach 5 applications. The paper summarizes the design methodology constructing fully 3D intake geometry from 2D axisymmetric flow templates, steamline tracing and boundary layer correction. The intake is tested at its design speed (Mach 5) and altitude (25000 m). Nonetheless the emphasis is placed on understanding the off-design behavior of such intake under varying different flight Mach number, altitude, angles of attack and sideslip angles, using RANS simulations to asses performance and stability.

2. Methodology

2.1. Intake Design

The intake design methodology is based on the integration of the Taylor-Maccoll equations for axisymmetric flow [2]. Under this assumption, the flow field reduces to a two-dimensional problem in polar coordinates (r, θ), eliminating the circumferential dependence. A numerical tool on MATLAB environment was developed to generate optimal 2D wall contours from input parameters including inlet Mach number M_1, exit Mach number M_3, and outlet radius r.

While Busemann intakes provide excellent isentropic compression performance, their excessive length increases skin friction drag, boundary layer development, and weight. To address this limitation, a truncation angle δ_t was introduced to remove the initial low-curvature section that contributes minimally to compression [12]. Although truncation generates a shock wave that disrupts the isentropic flow field, flow uniformity at the exit plane is restored by adding a flat plate inclined at the truncation angle. 2D CFD analysis showed that $\delta_t = 5°$ achieves a length reduction of approximately 22.5% with only 3.5% total pressure loss compared to the non-truncated design.

The inviscid Taylor-Maccoll formulation requires viscous corrections to account for boundary layer development, which compresses the flow field through displacement thickness effects and shifts the conical shock focal point upstream. To restore the inviscid flow topology, RANS simulations were performed with 200 wall-normal lines to extract pressure, velocity, density, and total enthalpy distributions for boundary layer thickness calculations and subsequent geometry adjustments [13].

The final step involves generating the 3D geometry from the corrected 2D profile. Since axisymmetric shapes may not integrate well with the overall vehicle structure, an elliptical cross-section with aspect ratio 3:1 was adopted. The streamline-tracing technique preserves flow characteristics while modifying the cross-sectional shape [14]. The wavecatcher configuration enhances intake starting during acceleration phases.

The 3D surface construction assembles scaled Busemann streamlines using the relationship $\bar{r} = y(\phi)f(\theta)$, where $f(\theta)$ represents the Busemann streamline profile, and $y(\phi)$ is a scaling factor. The angle τ defines the orientation between the z-axis and the line connecting the symmetry axis to points on the cross-sectional perimeter. The resulting Cartesian coordinates are given by equation below and final 3D intake geometry if presented in Fig. 1.

$$x = \bar{r}\cos(\theta), \quad y = \bar{r}\sin(\theta)\cos(\tau), \quad z = \bar{r}\sin(\theta)\sin(\tau) \tag{1}$$

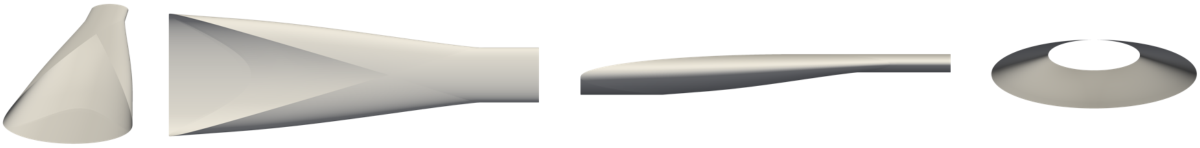

Fig 1. Final geometry of 3D truncated Busemann Intake (from left to right: oblique, top, side and frontal views)

2.2. Numerical Method

Computational fluid dynamics (CFD) simulations were performed to assess the on-design and off-design performance of the 3D Busemann intake. The Reynolds-Averaged Navier-Stokes (RANS) equations were solved using ANSYS Fluent with implicit time stepping and finite volume discretization. The AUSM flux scheme, well-suited for shock wave calculations, was employed alongside second-order upwind spatial discretization to enhance solution accuracy.

Several numerical acceleration techniques were implemented to improve computational efficiency. Full Multigrid (FMG) initialization provided superior initial solutions compared to standard initialization methods, significantly reducing convergence time. Solution steering enabled variable Courant numbers during iterations, starting with conservative values to minimize numerical errors and gradually increasing to accelerate convergence.

The simulations employed realistic atmospheric conditions corresponding to an altitude of 25 km, with temperature $T = 221.55$ K and pressure $P = 2511$ Pa. The design flight Mach number was set to $M_1 = 5$. An ideal gas model was assumed, and the k-ω SST turbulence model was used to close the RANS equations.

2.3. Computational Domain

Figure 2 provides the details of the boundary conditions and the arrangement of the computational domain as a whole. The boundary conditions consist of pressure far-field at the inlet with static pressure and temperature corresponding to 25 km altitude, and pressure outlet at the exit of the domain. For supersonic flow conditions, no back pressure specification is required at the outlet boundary.

Due to the geometric complexity, a watertight mesh approach was implemented using Fluent Meshing within the ANSYS software suite, as shown in Figure 3, providing superior element quality compared to traditional unstructured meshing tools. A detailed mesh convergence study was conducted to determine the minimum resolution required for grid-independent results. To accurately resolve boundary layer effects, an inflation layer with 25 layers in total was applied with first layer thickness of 1×10^{-5} m ensuring $y^+ < 1$ throughout the wall surfaces.

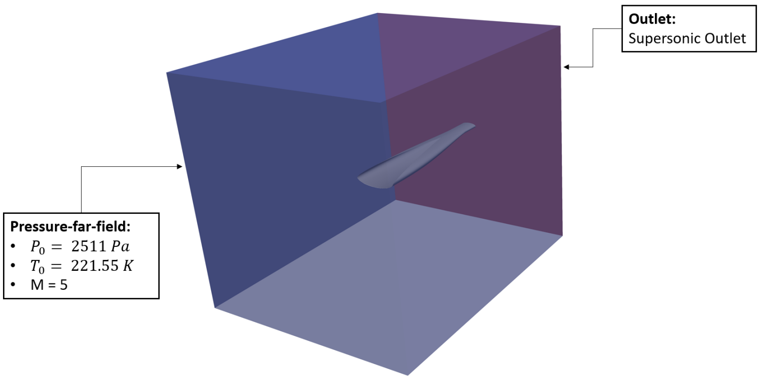

Fig 2. Computational Domain.

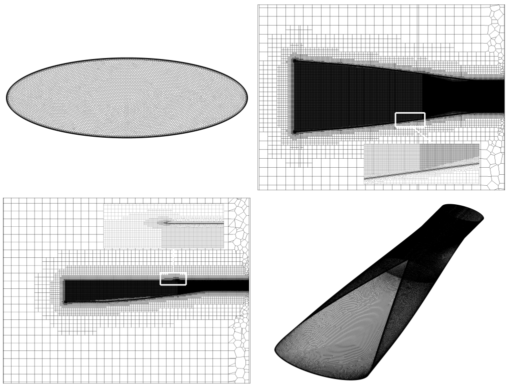

Fig 3. Mesh View.

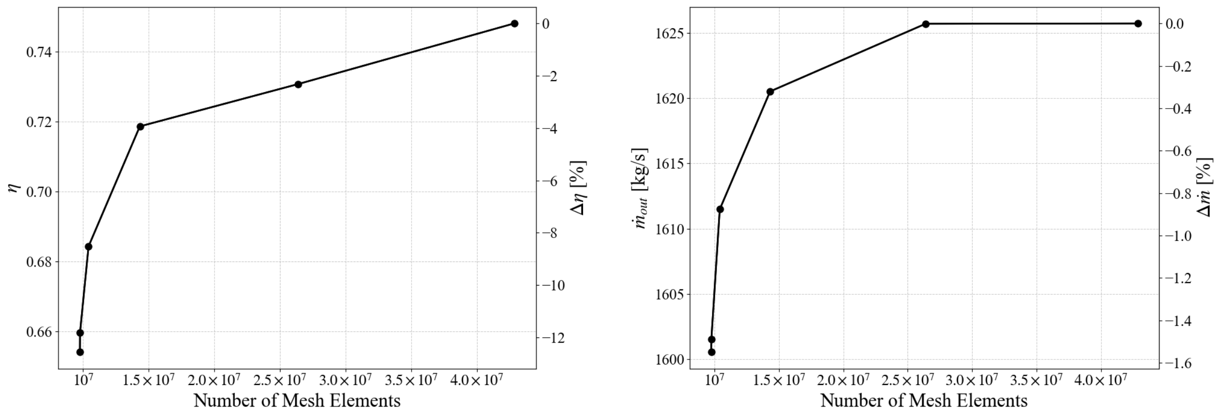

Fig 4. Compression efficiency $\left(\frac{p^0_{\text{out}}}{p^0_{\text{in}}}\right)$ and mass flow rate $(\dot{m})$ versus mesh element count, showing deviation from the finest mesh solution.

Figure 4 provides the summary of the mesh independency study conducted over 6 different meshes ranging from 10 to 50 million grid elements. The study demonstrates that compression efficiency is more sensitive to mesh resolution than mass flow rate through the intake. Balancing solution accuracy with computational cost, Mesh 5 containing approximately 26 million cells was selected for all simulations in this paper.

2.4. Boundary Layer Transition vs Fully Turbulent k-w model

Prior to conducting the design analysis, a comparative study was performed between turbulence models to assess the impact of boundary layer transition on intake performance. Specifically, a transition model that captures the laminar-to-turbulent transition was compared against a fully turbulent model to determine whether boundary layer transition significantly affects the aerodynamic characteristics of the hypersonic intake.

The comparison utilized the Transition SST 4-equation model, which predicts boundary layer transition, versus the standard k-ω SST model, which assumes fully turbulent conditions from the inlet. Figure 5 illustrates the intermittency distribution, a parameter that quantifies the degree of flow turbulence, where values of 0 and 1 correspond to fully laminar and fully turbulent conditions, respectively. At the operating altitude of 25 km, the atmospheric flow is predominantly laminar, and as shown in the figure, the transition to turbulent flow occurs downstream of the intake leading edge. This behavior contrasts with the k-ω SST model assumption of fully turbulent flow from the inlet.

However, analysis of the outlet flow conditions presented in Table 1 reveals that despite the k-ω SST model's inability to capture boundary layer transition physics, the predicted performance parameters

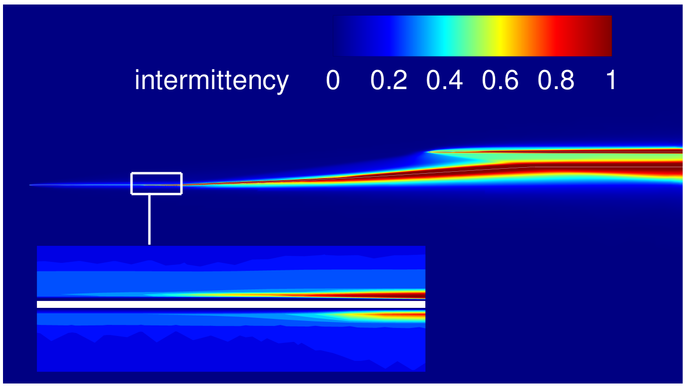

Fig 5. Intermittency distribution along the symmetry plane using Transition SST 4-equation model at 25 km altitude. Values range from 0 (fully laminar) to 1 (fully turbulent), showing boundary layer transition.

exhibit excellent agreement with those obtained using the transition model. The maximum deviation in key performance metrics was less than 2%, demonstrating that the fully turbulent assumption provides sufficient accuracy for this application.

Model	η	Mach	P **[Pa]**	$\dot{m}$ **[kg/s]**
Fully Turbulent	0.73	2.72	36816	1625
Transition	0.746	2.74	36486	1627
Δ [%]	2.14	0.73	0.90	0.12

Table 1. Comparison of outlet flow parameters between Transition SST 4-equation model and k-ω SST fully turbulent model at design conditions.

Consequently, the k-ω SST model was selected for the subsequent parametric studies due to its computational efficiency while maintaining acceptable accuracy levels. This approach enables extensive design space exploration without compromising result quality, making it well-suited for the comprehensive intake analysis presented in this work.

2.5. Test Matrix

Table 2 presents the comprehensive set of off-design conditions, along with the limit and variation steps, investigated in this study, examining the independent effects of altitude, flight Mach number, angle of attack, and sideslip angle variations.

Off-Design variable	**Range**	**Variation**
α	$-10° + 10°$	$2.5°$
β	$0 - 5°$	$1°$
M_{flight}	$3 - 6$	0.5
h	$15 - 30km$	$5km$

Table 2. Parametric study matrix covering flight Mach numbers (3–6), angles of attack ($-10°$ to $+10°$), and sideslip angles ($0°$ to $+5°$). Each marker represents an individual CFD simulation.

3. Baseline Results - Design Condition

The major on-design attributes of the flow field along the designed intake was extracted from the simulation at Mach 5 and 25 km of altitude and depicted in Figures 6 and 7.

Figure 6a shows the flow uniformity at the intake outlet plane in terms of the Mach number contours. A noticeable boundary layer development can be observed, which is more pronounced along the lower

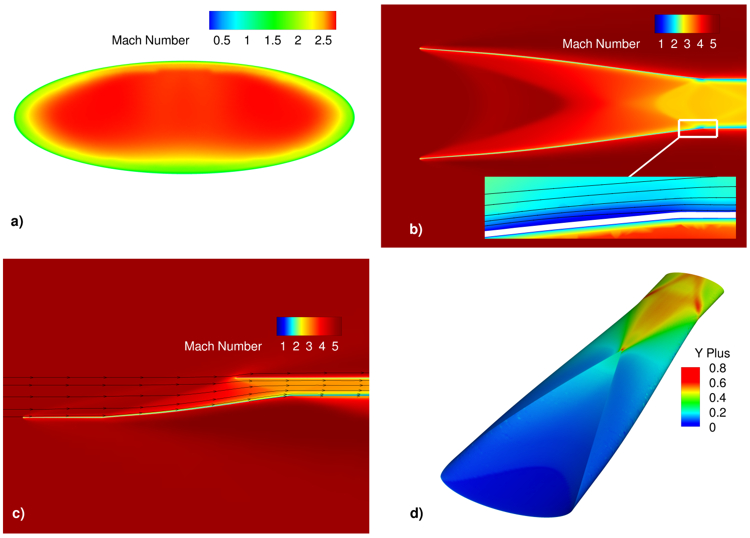

Fig 6. Mach number contours **a)** at the outlet section; **b)** on a transversal plane, with a zoomed view of the intake bend; **c)** on the symmetry plane; **d)** y^+ distribution along the internal wall of the intake.

wall than the upper wall due to the extensively longer distance that the flow has to travel as compared to upper wall. This asymmetry results from the intake geometry, having a longer surface where the boundary layer can grow in the bottom side.
Figures 6b and 6c present Mach number contours on a transverse plane and the axial symmetry plane, respectively. These plots highlight the progressive flow compression induced by the intake geometry. In particular, these Figures show the 3D shock structure impingement on the wall corner without any evidence of flow separation, as confirmed by the streamline pattern. Furthermore, the streamline behaviour near the notch indicates the presence of slight mass flow spillage even under on-design conditions, which helps prevent the occurrence of buzz instability. The shock-induced flow deflection, combined with the intake geometry, ensures that the flow enters the isolator nearly parallel to the intake walls. Finally, 6d displays the y^+ distribution on the internal wall surface of the intake. The maximum y^+ value is approximately 0.6, occurring near the shock impingement and reflection points, and remains below the critical threshold of $y^+ < 1$, thereby ensuring accurate resolution of the boundary layer along the walls of the intake.

Prominent flow structures created by the intake are shown in Figure 7 through pressure iso-surfaces, Schlieren visualizations as well as the total pressure recovery distribution at the outlet plane. Figure 7a displays the three-dimensional shock-wave system, highlighting the first oblique shock generated by the initial truncation, as well as the conical shock and its subsequent reflections. In particular, the conical nature of the first two shock waves can be clearly observed. Figures 7b–c present the two-dimensional flow-field structures using Schlieren visualization, where the initial shock, the isentropic compression region, and the conical shock with its wall reflection are visible.

Finally, Figure 7d depicts the total pressure recovery, which quantifies the intake's compression efficiency at the outlet plane. The most significant viscous losses are concentrated along the lower and side walls, where the boundary layer experiences much longer path to develop. Conversely, the upper wall near the crotch exhibits smaller losses due to the reduced surface area available for boundary-layer to grow. In the central core region, the total pressure recovery remains relatively uniform, with values around 0.96. This indicates that the dominant losses in this area are caused by shock waves, confirming the effectiveness of the shock-based compression system.

By examining the mass-weighted average values reported in Table 3, the increased complexity of the intake in the 3D case becomes evident compared to the simpler 2D configuration. Notably, the average efficiency at the outlet decreases to approximately 0.73 in the 3D case, whereas in the 2D viscous simulation it reached values as high as 0.87. This reduction highlights both the geometric and physical

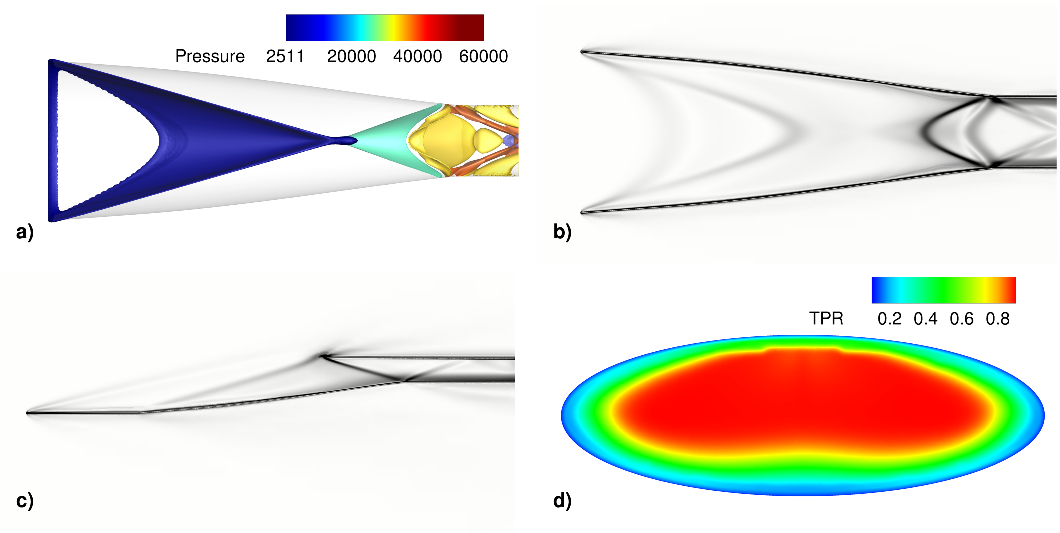

Fig 7. a) 3D iso-Surfaces shochwave structure, **b-c)** Schliren visualization for the transversal and symmetric plane respectively, **d)** total pressure recovery distribution at the outlet plane

complexity of the 3D intake, as well as the compromises introduced by modifying the intake cross-section. Specifically, the shape is no longer axisymmetric but elliptical, a change that led to increased total pressure losses and a stronger compression. This is evidenced by a higher static pressure and a lower Mach number at the outlet, compared to the ideal design condition with a downstream Mach number of $M_3 = 3$.

Mach Number [-]	**Static Pressure** [Pa]	**Mass-flow rate** [kg/s]	**TPR** [-]	**Capture Efficiency** [-]
2.72	36816	1625	0.7307	0.9916

Table 3. Mass-weighted averages of key flow parameters—mass flow rate, static pressure, Mach number, Total Pressure Ratio and Capture Efficiency evaluated at the outlet section.

4. Off-Design Analysis

4.1. Effect of Angle of Attack (α) Variation

A preliminary assessment of intake performance as a function of angle of attack is shown in Figure 8. It can be observed that, in general, increasing or decreasing the angle of attack from the on-design condition ($\alpha = 0°$) leads to a deterioration in performance. An exception is found at $\alpha = -2.5°$, where a slight increase in compression efficiency is observed. The trend in mass flow rate with respect to angle of attack reveals that negative angles result in an increase in mass flow rate, while positive angles lead to a decrease. This behavior can be attributed to changes in the effective capture area, given that the freestream Mach number is held constant. For negative angles of attack, the capture area increases, whereas for positive angles, it decreases. This is primarily due to the intake geometry, which features an opening in the upper region. When the intake is inclined downward (negative α), this upper opening becomes more exposed to the incoming flow, effectively enlarging the apparent intake area. This geometric effect is illustrated in Figures 9 and 10.

Continuing the analysis of performance parameters in Figure 8, it can be observed that, in addition to the variation in mass flow rate with angle of attack, both static pressure and Mach number exhibit similar trends. Specifically, for negative angles of attack—where a larger amount of air is captured by the intake—the flow undergoes greater compression, as evidenced by the increase in outlet static pressure, and experiences a stronger deceleration, as shown by the reduction in Mach number. Conversely, at positive angles of attack—where the effective capture area is reduced—the intake captures less air,

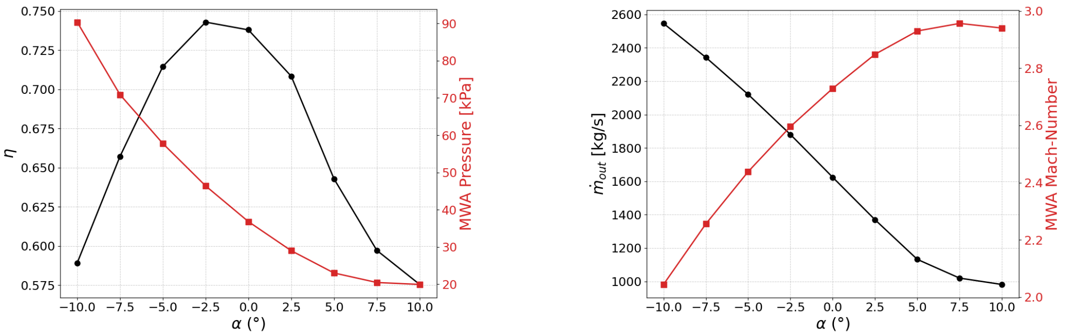

Fig 8. Effect of angle of attack (α) variation on the mass-weighted average outlet values: compression efficiency and static pressure (left), Mach number and mass flow rate (right).

resulting in lower compression and less deceleration of the flow.

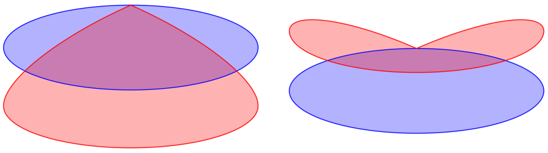

Fig 9. Effect of angle of attack on the intake capture area. The baseline capture area at $\alpha = 0°$ is shown in blue; deviations at negative α are shown in red on the left, and at positive α in red on the right.

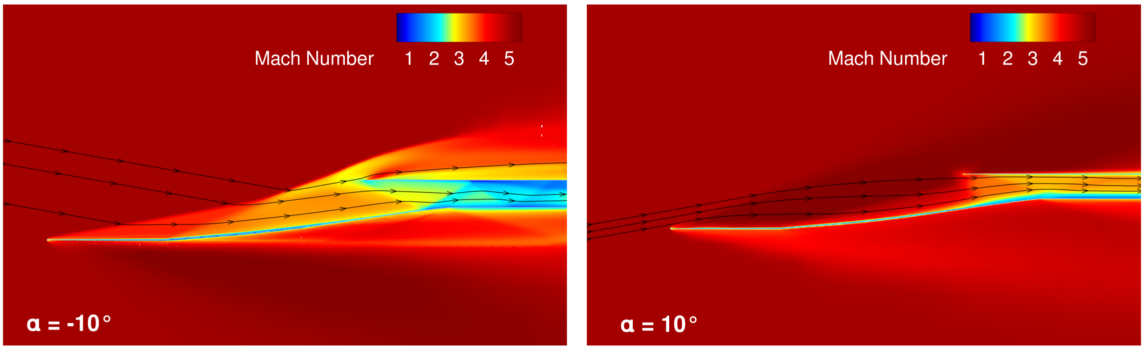

Fig 10. Mach number contours along the intake symmetry plane for $\alpha = 10°$ and $\alpha = -10°$, illustrating the velocity streamlines.

A comparison of the flow-field structures for the two extreme cases, $\alpha = 10°$ and $\alpha = -10°$, is presented in Figures 11. The Mach number contours at the outlet reveal that positive angles of attack preserve flow distortion similar to the on-design case, including the presence of vortices near the lateral walls. In contrast, at negative angles of attack, the outlet flow structure changes significantly, with vortices forming along the centerline. This behavior is also evident in Figure 11d, where a vortex originating from the side wall, much upstream, develops toward the intake's main axis and dominates the outlet flow area.

Despite the significant flow modifications observed, it is important to highlight that the intake does not exhibit the unstart phenomenon, even under extreme angles of attack. This result is particularly relevant, as operating at negative α values plays a crucial role in scenarios where the intake has become unstarted. In such cases, the vehicle must adopt a negative angle of attack to maximize the captured airflow and promote re-starting of the intake as quickly as possible. Therefore, the intake's ability to maintain attached flow and avoid unstart under these off-design conditions represents a key advantage in terms of operational stability and recovery strategies.

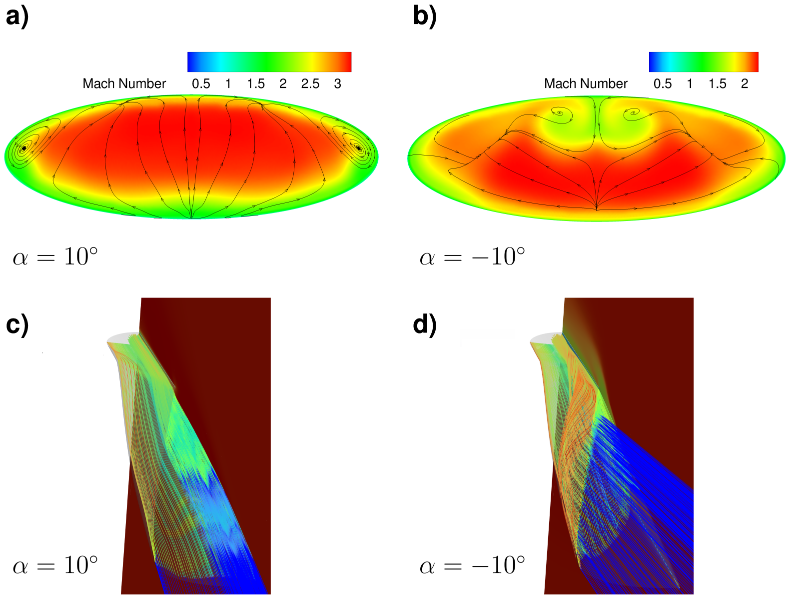

Fig 11. Comparison of flow-field structures at $\alpha = 10°$ and $\alpha = -10°$: Mach number contours at the outlet **(a–b)**, and streamlines colored by vorticity magnitude **(c–d)**.

4.2. Effect of Sideslip Angle (β) Variation

The influence of sideslip angle (β) variation on intake performance is presented in Figure 12, where trends of mass flow rate, efficiency, and the mass-weighted average values of Mach number and static pressure at the outlet are reported.

Only positive values of β are considered, as the intake geometry is symmetric with respect to the x-z plane. Consequently, negative sideslip angles would produce mirrored, and thus equivalent, results due to the symmetry of the configuration.

It is immediately evident that, unlike angle of attack variations, the mass flow rate remains nearly constant with increasing sideslip angle. This suggests that the effective capture area is not significantly affected by β, in contrast to its strong sensitivity to α variations.

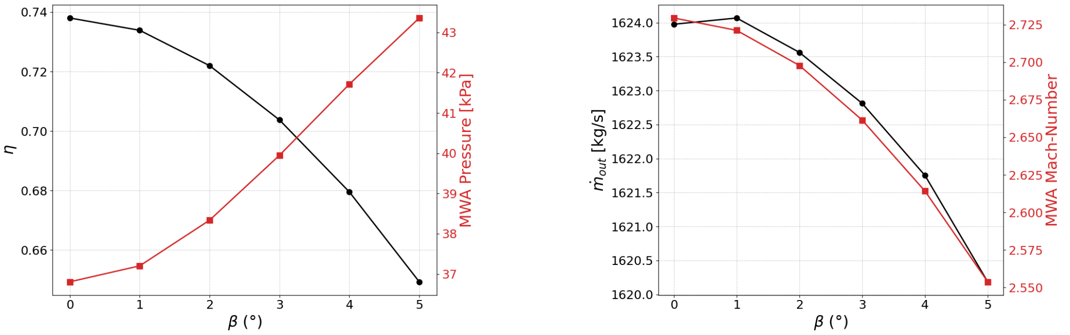

Fig 12. Effect of angle of sideslip (β) variation on the mass-weighted average outlet values: compression efficiency and static pressure (left), Mach number and mass flow rate (right).

However, other performance parameters show notable variations. In particular, an increase in β leads to a degradation of overall performance and an increase in asymmetric flow compression. This is reflected in the rise of static pressure at the outlet and the decrease in Mach number, indicating a stronger deceleration of the flow. These observations imply a modification of the shock structure and compression pattern compared to the on-design condition. As shown in Figure 13, the compression structure changes significantly under sideslip conditions. In particular, the Schlieren visualization on the transverse plane in Figure 13b reveals the loss of the isentropic compression pattern observed in the on-design case. Instead, an oblique shock forms and impinges on the side wall. In the zoomed view in Figure 13d, focusing on the shock impingement region, a strong interaction between the shock wave and the boundary layer can be observed. This interaction leads to boundary layer separation and the formation of vortices, as highlighted by the streamlines. These features contribute to a loss in total pressure and, consequently, efficiency.

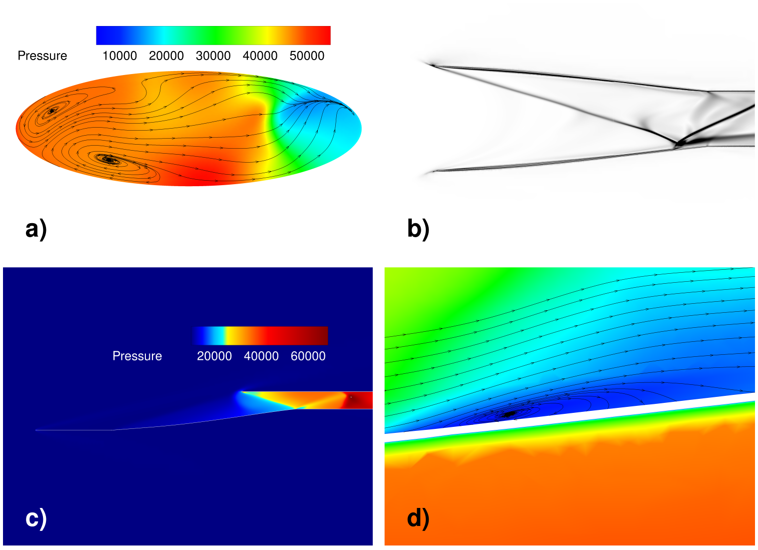

Fig 13. Comparison of flow-field structures at $\beta = 5^\circ$: **(a)** pressure contour at the outlet section; **(b)** Schlieren visualization on a transversal plane; **(c)** pressure contour on the symmetry plane; **(d)** zoomed view of the intake bend highlighting the strong shock–boundary-layer interaction.

In the Figure 13a, the static pressure contour at the outlet shows a markedly different structure compared to the on-design configuration. The flow appears more compressed on the left-hand side of the outlet where the reflected shock wave propagates, and vortical structures are again dominant, negatively affecting flow uniformity at the exit. The Figure 13c, showing the symmetry plane, indicates a sudden pressure rise near the end of the isolator, likely caused by the reflection of the wall-bounded shock wave.

Despite these significant changes in the internal flow structure, it is important to note that the intake does not experience unstart similar to the cases under angle of attack variation. This suggests that for small sideslip angles, the intake remains stable and functional. Given the high-speed flight conditions typical of this engine configuration, where large sideslip maneuvers are uncommon, this result is particularly relevant. It confirms that the intake design can tolerate small deviations in β without flow breakdown, maintaining operational robustness.

4.3. Effect of Freestream Mach Number (M_∞) Variation

Figure 14 presents the effects of varying the freestream Mach number on key performance parameters, namely the mass flow rate, compression efficiency, and the mass-weighted average values of Mach number and static pressure at the outlet. The first notable observation is that, as the flight Mach number decreases to $M_\infty = 3$, the intake exhibits an unstarted behavior. This is primarily due to the specific geometry of the intake and the area ratio between the inlet and outlet in the studied design.

The mass flow rate shows an approximately linear trend with respect to the flight Mach number: as the

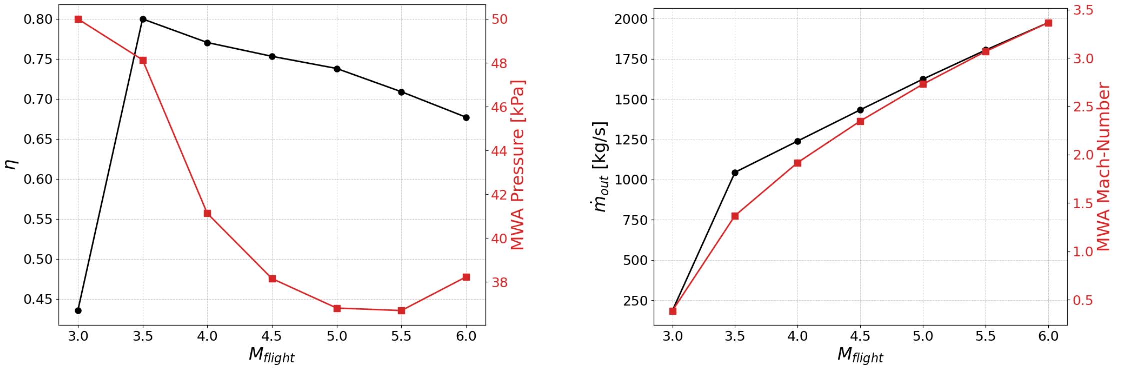

Fig 14. Effect of flight Mach Number (M_∞) variation on the mass-weighted outlet values: compression efficiency and static pressure (left), Mach number and mass flow rate (right).

Mach number increases, more air is ingested by the intake, and vice versa. This aligns with physical expectations. Regarding the static pressure, it is observed that higher flight Mach numbers do not significantly alter the compression system. According to shock wave theory, as the Mach number increases, the shock angle becomes more oblique, allowing the shock to extend further downstream, which results in some of the incoming air entering the intake without being compressed, as it can be seen in Fig 14. Despite this, the increased velocity results in greater compression, which also leads to higher total pressure losses, as reflected by a decrease in compression efficiency.

At lower flight Mach numbers, the flow experiences an overboard spillage phenomenon, wherein the percentage of captured mass is reduced. This is due to the fact that, at lower Mach numbers and fixed geometry, the shock wave becomes less inclined and deflects the flow more strongly, thereby reducing the effective capture area. Nevertheless, a higher efficiency is observed at these lower Mach numbers. This indicates that the total pressure losses are smaller in this regime, but in turn the intake processing a lower mass flow and compresses it more effectively, which explains the rise in outlet pressure.

The efficiency value at $M_\infty = 3$ should be interpreted as a time-averaged quantity, since under this flight condition the shock wave does not reach a steady position but oscillates, demonstrating the unsteady behavior of the intake in the unstarted configuration.

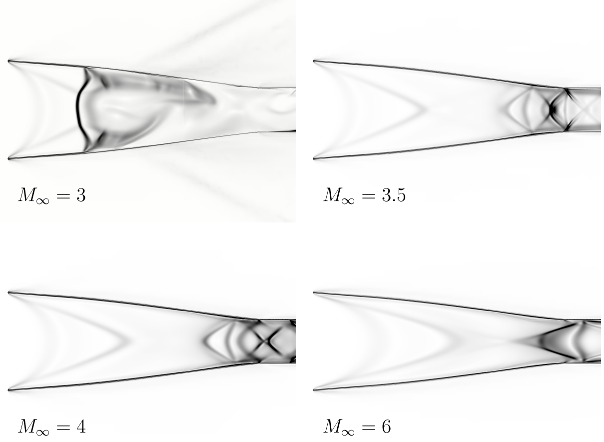

Fig 15. Schlieren contours illustrating the evolution of the compression shock structure for different freestream Mach numbers.

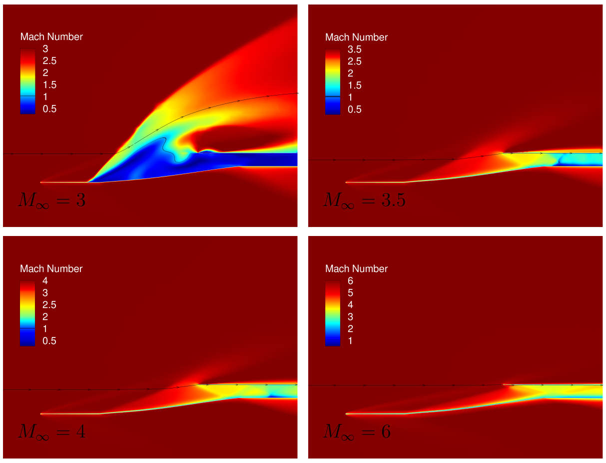

Fig 16. Mach number contours along the symmetry plane for different freestream Mach numbers. Velocity streamlines are included to illustrate the overboard spillage phenomenon at lower Mach numbers. A black contour line is used to indicate the locus of Mach number equal to 1.

The Schlieren visualizations in Figure 15 illustrate how the shock wave structure evolves with different freestream Mach numbers. Specifically, it can be observed that as the Mach number decreases (e.g., $M_\infty = 4$, 3.5, and 3), the shock waves tend to move upstream and widen, due to the increased amount of spillage occurring at lower speeds.

In contrast, at higher freestream Mach numbers (e.g., $M_\infty = 6$), the shock system appears more elongated and shifts downstream along the intake. This behavior is consistent with shock wave theory, which predicts that as the Mach number increases, shock waves become more oblique and are deflected further downstream.

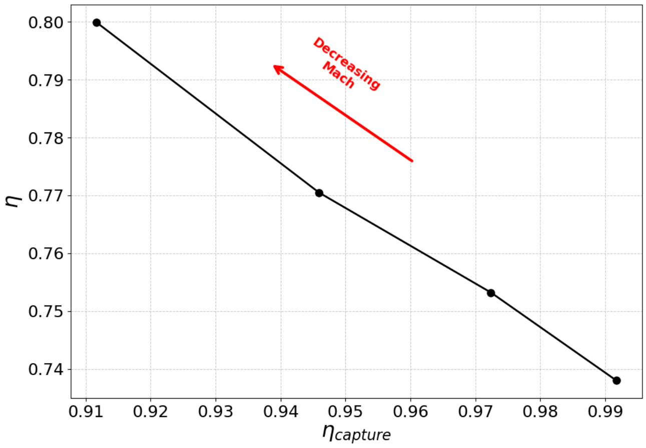

Fig 17. Capture efficiency versus total pressure recovery for different flight mach numbers

Figure 17 presents the total pressure recovery as a function of capture efficiency. As previously anticipated, a decrease in the flight Mach number leads to reduced mass-flow capture and increased overboard spillage, while simultaneously producing a higher total pressure ratio. The unstarted condition is excluded from the plot due to its low total pressure efficiency, in order to improve the clarity of the results.

4.4. Effect of Altitude (h) Variation

Finally, the effect of altitude variation is simulated by varying atmospheric properties using ISA table values between 15 and 30 km by 5 km steps. Figure 18 illustrates the total pressure recovery as a function of mass capture efficiency for different altitudes. The results indicate that altitude has only a minor influence on capture efficiency, with slight variations observed between 10 km and 30 km, as compared to other off-design variations. In contrast, the overall total pressure recovery decreases with altitude.

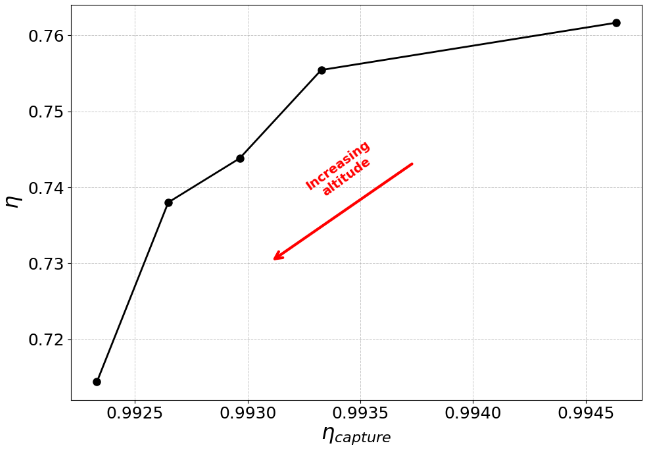

Fig 18. Capture efficiency versus total pressure recovery for different altitudes

At higher altitudes, where pressure, temperature, and density are lower, the intake system compresses the air less efficiently. However, the reduced density also decreases the available mass flow, and consequently, the potential thrust generated by the engine. Therefore, altitude must be carefully considered when maximizing intake efficiency is a design objective.

5. Conclusions

A methodology to design highly 3D stream-traced hypersonic intakes was outlined for a dual-mode ramjet engine to operate at Mach 5 curise conditions. A Busemann intake was selected due to its superior performance compared to the Oswatitsch and Prandtl–Meyer configurations. Initially, two-dimensional analyses accounting for boundary-layer contraction were conducted to biuld the axisymmetric intake profile and to evaluate possible reductions in intake length. Based on these results, a three-dimensional intake model was generated using a stream-tracing design methodology. The final intake was simualted at design conditons to understand the main flow features and quantify the behavior of the geometry. Off-design simulations were then performed by independently varying the angle of attack (α), sideslip angle (β), flight Mach number, and operational altitude. Both the flow-field structures and the outlet performance parameters were analyzed. The highest sensitivity of the flow field to the changing conditions is found at varying angle of attack and flight Mach number. Overall, the results demonstrate that this intake configuration maintains good performance across a wide range of off-design conditions, indicating a robust operational envelope for future hypersonic flight applications.

Acknowledgements

The MORE LESS project leading to this publication has received funding from the European Union's Horizon 2020 Framework Programme for Research and Innovation under grant agreement number 101006856.

References

[1] M. K. Smart, “Scramjet inlets,” in RTO-EN-AVT-185, NATO Research and Technology Organisation (RTO), 2014.

[2] S. Mölder, “The busemann air intake for hypersonic speeds,” in Hypersonic Vehicles - Past, Present and Future Developments (G. Pezzella and A. Viviani, eds.), IntechOpen, 2019.

[3] S. E. Molder, “Busemann inlet for hypersonic speeds,” Journal of Spacecraft and Rockets, 1966.

[4] D. V. Wie and M. S., “Application of busemann inlet designs for flight at hypersonic speeds,” in Aerospace Design Conference, no. AIAA 92-1210, American Institute of Aeronautics and Astronautics (AIAA), 1992.

[5] J. B. Keirsey, C. B., and S. M. L., “Design and test evaluation of a three module hypersonic inlet,” Tech. Rep. TG-699, Johns Hopkins University, Applied Physics Laboratory (APL/JHU), 1965.

[6] A. J. T. Matthews, “Design and test of a modular waverider hypersonic intake,” tech. rep., Department of Engineering Science, Oxford University, 2003.

[7] S. D. K. H. Johan Steelant, Richard Varvill and M. Marini, “Achievements obtained for sustained hypersonic flight within the lapcat-ii project,” in 20th AIAA International Space Planes and Hypersonic Systems and Technologies Conference, (Glasgow, Scotland, UK), 2015.

[8] J. Steelant, “Sustained hypersonic flight in europe: First technology achievements within lapcat ii,” in 17th AIAA International Space Planes and Hypersonic Systems and Technologies Conference, 2012.

[9] P. R. P. N. T. Langener, J. Steelant and M. Marini, “Preliminary performance analysis of the lapcat-mr2 by means of nose-to-tail computations,” in 18th AIAA/3AF International Space Planes and Hypersonic Systems and Technologies Conference, 2012.

[10] B. S. C. S. V. G. J. M. M. M. S. H. K. L. A. V. D. H. B. L. F. L. C. F. Nicole Viola, Roberta Fusaro, “Main challenges and goals of the h2020 stratofly project,” 2021.

[11] K. Van den Borre, A. C. Ispir, B. O. Cakir, and B. H. Saracoglu, Reduced Order Computational Methods for the Development of Propulsive Technologies for Supersonic Aviation to Achieve Climate Neutrality, pp. 95–107. Springer International Publishing, 2024.

[12] Z. Zhao and W. Song, "Effect of Truncation on the Performance of Busemann Inlet," Modern Applied Science, vol. 3, Jan. 2009.

[13] P. C. Walsh, R. B. Tahir, and S. Molder, "Boundary-layer Correction for the Busemann Hypersonic Air Inlet," Canadian Aeronautics and Space Journal, vol. 49, pp. 11–17, Mar. 2003.

[14] M. Smart., "Design of three-dimensional hypersonic inlets with rectangular to elliptical shapre transition," in Hypersonic Airbreathing Propulsuion Branch, American Institute of Aeronautics and Astronautics, Feb. 1998.